Letter

Helical boundary modes from synthetic spin in a plasmonic lattice

Sang Hyun Park,[1] Michael Sammon,[1] E. J. Mele,[2] and Tony Low[1,*]
[1]*Department of Electrical and Computer Engineering, University of Minnesota, Minneapolis, Minnesota 55455, USA*
[2]*Department of Physics and Astronomy, University of Pennsylvania, Philadelphia, Pennsylvania 19104, USA*

(Received 29 May 2023; revised 7 March 2024; accepted 25 March 2024; published 22 April 2024)

Artificial lattices have been used as a platform to extend the application of topological band theory beyond electronic systems. Here, using the two-dimensional Lieb lattice as a prototypical example, we show that an array of disks which each support localized plasmon modes gives rise to an analog of the quantum spin-Hall state enforced by a synthetic time-reversal symmetry. We find that the plasmonic modes naturally possess a synthetic spin degree of freedom which leads to a spin-dependent second-neighbor coupling mechanism mediated by interorbital coupling. This interaction introduces a nontrivial Z_2 topological order and gaps out the Bloch spectrum. A faithful mapping of the plasmonic system onto a tight-binding model is developed and shown to capture its essential topological signatures. Full wave numerical simulations of graphene disks arranged in a Lieb lattice confirm the existence of propagating helical boundary modes in the nontrivial band gap.

DOI: 10.1103/PhysRevB.109.L161301

Introduction. Artificial lattices can be patterned into ordered structures designed to control the efficient flow of energy and information [1]. There has been particular interest in developing periodic structures for this purpose that use nontrivial topology in their interior Bloch bands [2,3]. These are known to support protected transport channels at boundaries between distinct topological states, in analogy to the well-studied electronic surface states that occur at the boundaries of two- and three-dimensional topological insulators [4]. Indeed, nontrivial bulk Chern bands in two dimensions have been successfully developed on photonic [5], plasmonic [6], and even mechanical platforms [7], where time-reversal symmetry is broken in order to establish their topological nature. In striking contrast, photonic two-dimensional (2D) analogs to quantum spin-Hall states which retain time-reversal symmetry have been elusive. A key challenge is that the Kramer's degeneracies for half-integral angular momentum, whose connectivity is essential for defining the topological state, are generically absent from photonic and plasmonic analogs [8]. While multiple realizations of a photonic quantum spin-Hall state have been demonstrated [9–11], intricate engineering via fine tuning of the design is required to enforce the required symmetries [3].

In particular, graphene has been proven to be a promising platform for realizing topological plasmons due to its highly controllable carrier density. Spatially varying modulations to the carrier density achieved by patterning [6,12] or introducing a metagate [13,14] folds the plasmon dispersion into a plasmonic band structure where the addition of time-reversal symmetry-breaking magnetic fields or mirror symmetry-breaking chemical potentials can open topologically nontrivial gaps. Propagating edge plasmon modes are observed in the topologically nontrivial gaps. However, such realizations of a plasmonic crystal lack natural spin degrees of freedom, making it difficult to realize analogs of the quantum spin-Hall effect which gives rise to counter-propagating helical edge states without having to introduce symmetry breaking. Furthermore, proposed plasmonic crystals developed by imposing weak density modulations on a uniform background charge density are lacking the flexibility to engineer lattice networks with topological character.

In this Letter, we suggest a different approach to this problem and illustrate it with studies of a two-dimensional plasmonic Lieb lattice [15,16] as a prototype. We construct the plasmonic lattice by analyzing an array of graphene nanodisks in a Lieb lattice configuration, where each disk is a local resonator that supports a ladder of localized plasmon modes. The rotational symmetry of the disks gives rise to synthetic spin degrees of freedom for the localized plasmons. Interestingly, we identify an interorbital interaction between different multipole sectors that leads to an effective spin-dependent second-neighbor coupling. The effective coupling mechanism is shown to open a topologically nontrivial gap in the plasmon band structure with spin-polarized edge plasmon modes traversing the gap. Our model is characterized by two length (energy) scales that express the confinement of excitations within and transmission between nodes of a Lieb lattice network. Over a realizable parameter range in which these scales are of comparable size, we identify both an emergent twofold Kramer's degeneracy and a synthetic spin-orbit process that gaps the Bloch spectra to endow the bands with nontrivial Z_2 topological order [17]. We test this idea with full wave numerical calculations to confirm the existence of counter-propagating helical modes on the boundaries. We emphasize that these phenomena in artificial lattices are controlled by two energy scales which are tunable over a wide dynamic range and access ordered states that are practically unachievable in

*tlow@umn.edu

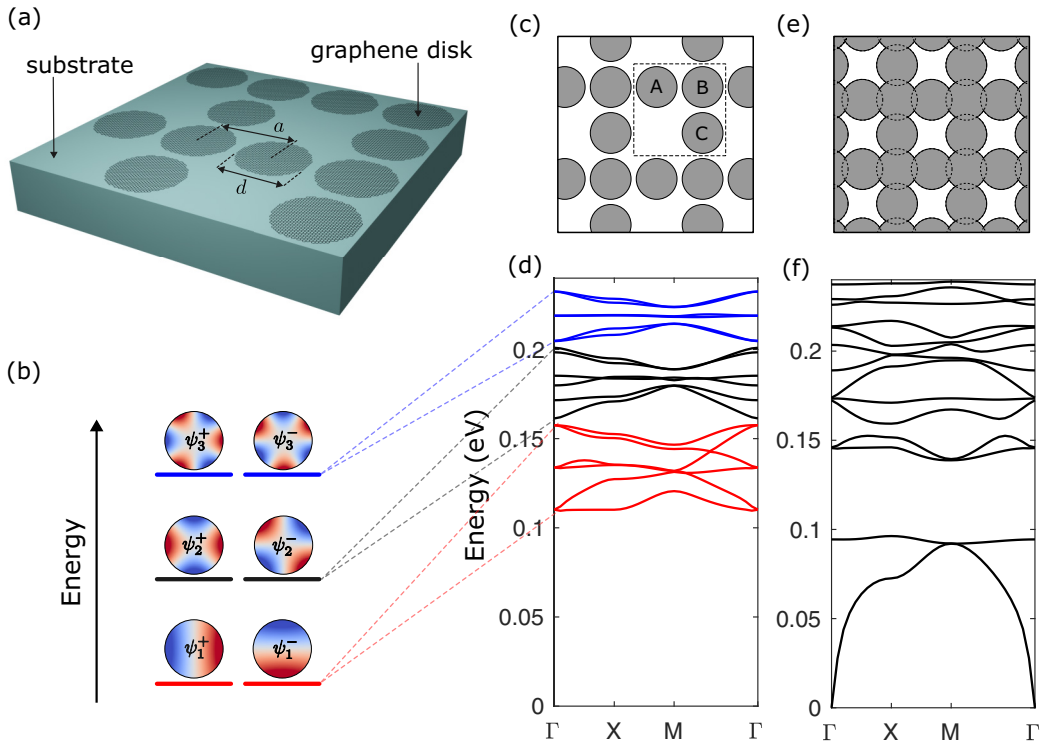

FIG. 1. Plasmonic band structure of graphene nanodisk arrays. (a) Schematic representation of an array of graphene disks configured into a Lieb lattice. (b) Electric potential of the first six plasmonic modes of an isolated graphene disk. (c) Top-down view of the plasmonic Lieb lattice with $d = 100$ nm and $a = 105$ nm. The dashed box shows the unit cell of the lattice. (d) Plasmonic band structure corresponding to the arrangement shown in (c). The red, black, and blue bands correspond to bands formed by the dipole, quadrupole, and hexapole modes, respectively. (e) Top-down view of the plasmonic lattice with overlapping disks ($d = 100$ nm, $a = 85$ nm). Color coding of the bands is not applied since classification in terms of the multipole modes of the disk does not hold in this case. For all simulations, the graphene Fermi energy is set to $E_F = 0.5$ eV and the substrate dielectric constant is $\epsilon_s = 2.2$.

ordinary electronic materials. This strategy can be generalized to a wide family of appropriately designed artificial lattices.

Results and discussion. A plasmonic band structure can be calculated when graphene nanodisks are arranged in a periodic configuration [see Fig. 1(a)] where the localized plasmon modes of each disk will form a basis for the plasmonic band structure. The first six modes of an isolated graphene disk, shown in Fig. 1(b), are doubly degenerate dipole, quadrupole, and hexapole modes. The degeneracy of the multipole modes is enforced by the rotational symmetry of the nanodisks and will be shown to act as synthetic spin degrees of freedom in a plasmonic lattice. In this Letter, we will focus primarily on the bands formed by hopping between the quadrupole modes. Unlike the dipole and hexapole modes, the quadrupole modes do not couple to free space light and will have significantly lower losses. Note that while we use graphene plasmons due to their intrinsic two-dimensionality and tunable carrier density, any material that supports two-dimensional multipole modes will also be suitable for the proposal given in this work.

Here we analyze graphene nanodisks on a Lieb lattice [15,16] which shares the C_4 symmetry of the quadrupole modes. A spinless nearest-neighbor tight-binding model of the Lieb lattice has three bands, with a flat band in the middle and a threefold degeneracy at the M point where all three bands cross. Including spin degrees of freedom will double the number of bands and also induce a gap opening at the M point if a spin-dependent interaction is included [15]. The plasmonic band structure of the graphene disk Lieb lattice is shown in Fig. 1(d), where the disk diameter is set to $d = 100$ nm and the disk separation is $a = 105$ nm. The three groups of bands, colored in red, black, and blue, correspond to the bands formed by the dipole, quadrupole, and hexapole modes, respectively. We find that the dipole, quadrupole, and hexapole modes develop a band structure resembling the band structure of a tight-binding Lieb lattice. Interestingly, a gap opening is observed at the M point for the quadrupole and hexapole bands, which will be shown to be the result of a synthetic spin-dependent interaction. When the disks begin to overlap [$a < d$, Fig. 1(c)], a stark change in the band structure is observed. A low-energy hydrodynamic plasmon mode for which the dispersion satisfies $\omega \to 0$ as $q \to 0$ appears and the mapping onto a tight-binding Lieb lattice breaks down. This situation corresponds to the setup given in previous works [6,13,14,18], where periodic modulation of the structure or density is used to perturb the hydrodynamic mode.

To better understand the plasmon band structure given in Fig. 1(b), we develop a mapping of the plasmonic crystal onto a tight-binding model. The governing equations of the plasmonic response can be written as an eigenvalue equation

$\hat{H}\psi = \omega\psi$, where [6]

$$\hat{H} = \begin{pmatrix} 0 & \hat{V}\hat{\mathbf{p}}^T\sqrt{\omega_F(\mathbf{r})} \\ \frac{e^2}{\pi\hbar}\sqrt{\omega_F(\mathbf{r})}\hat{\mathbf{p}} & 0 \end{pmatrix}, \quad \psi = \begin{pmatrix} \Phi \\ \mathbf{J}/\sqrt{\omega_F(\mathbf{r})} \end{pmatrix}. \tag{1}$$

The eigenstate ψ is a vector of the potential Φ and current density $\mathbf{J}$, $\hat{\mathbf{p}}$ is the in-plane momentum operator, $\hat{V}$ is the Coulomb operator, and $\omega_F = E_F/\hbar$ is the Fermi frequency. The localized plasmonic modes of the nanodisk play the role of the atomic orbitals in a tight-binding theory. From an eigenmode calculation of the isolated graphene disk, we find that the electric potential is given by

$$\Phi^p_{n,l}(\mathbf{r}) = \begin{cases} u_n(r)\cos(l\theta), & p = + \\ u_n(r)\sin(l\theta), & p = -, \end{cases} \tag{2}$$

where $u_n(r)$ gives the radial dependence of Φ, n is the number of nodes in $u_n(r)$, and l is a positive integer. The six lowest-energy modes have $n = 0$ and $l = 1, 2, 3$, which correspond to the dipole ($l = 1$), quadrupole ($l = 2$), and hexapole ($l = 3$) modes. Henceforth, the superscript n will be omitted for notational simplicity. Note that rotational symmetry of the isolated graphene disk implies that ψ_l^+ and ψ_l^- are degenerate in energy (see Supplemental Material [19]).

Equipped with the Hamiltonian and atomic orbitals, we may now calculate the site diagonal and intersite matrix elements of the tight-binding Hamiltonian. In general, the matrix elements between orbitals ψ_l^p and $\psi_{l'}^{p'}$ on disks separated by $\mathbf{R}$ are given by

$$t_{ll'}^{pp'}(\mathbf{R}) = -i\frac{e^2}{\pi\hbar}\int \left[\mathbf{J}_l^{p*}(\mathbf{r})\cdot\nabla\Phi_{l'}^{p'}(\mathbf{r}-\mathbf{R}) + \Phi_l^{p*}(\mathbf{r})\nabla\cdot\mathbf{J}_{l'}^{p'}(\mathbf{r}-\mathbf{R})\right]d^2r, \tag{3}$$

where the inner product is defined such that $\hat{H}\psi = \omega\psi$ is a Hermitian eigenproblem [6]. With the current density and electric potential of the orbital modes, it is straightforward to calculate the tight-binding model parameters. For the Lieb lattice, the nearest-neighbor (NN) hopping parameters can be calculated by setting $\mathbf{R} = \pm a\hat{\mathbf{x}} \equiv \pm\mathbf{a}_x$ or $\mathbf{R} = \pm a\hat{\mathbf{y}} \equiv \pm\mathbf{a}_y$ in Eq. (3).

We now take a closer look at the nearest-neighbor coupling between the quadrupole orbitals $\psi_2^\pm$. Either by explicit calculation through Eq. (3) or by inspection of the mode symmetries, it may be shown that hopping from ψ_2^+ to ψ_2^- given by $t_{22}^{+-}(\mathbf{a}_j)$ is zero for $j = x, y$. It follows from the C_4 symmetry of the quadrupole modes that hopping magnitudes in the x and y directions will be equal, i.e., $t_{22}^{pp}(\mathbf{a}_x) = t_{22}^{pp}(\mathbf{a}_y)$ for $p = \pm$. Finally, it is important to note that the ψ_2^+ and ψ_2^- orbitals have hopping amplitudes with opposite sign. The plasmonic band structure of the quadrupole with nearest-neighbor hopping will therefore have two copies of the the three-band Lieb lattice band structure, where one of the copies will be inverted in energy with respect to the other. This is indeed what we observe for the quadrupole modes, as shown in Fig. 1(d). A similar analysis can be applied to the other multipole modes.

In order to understand the gap opening observed at the M point, we extend the model to include orbital coupling between the quadrupole modes ($\psi_2^\pm$) and the hexapole mode ψ_3^+. In Fig. 2(a), all allowed hoppings between the ψ_3^+ and $\psi_2^\pm$ modes are shown along with their respective signs. Hopping parameters $t_{23}^{++}(\pm\mathbf{a}_y)$, $t_{23}^{-+}(\pm\mathbf{a}_x)$ are zero and are not shown. Applying a C_4 rotation centered on the ψ_{+3} mode transforms the configuration of Figs. 2(a) into 2(b) with an overall sign change on all sites. This transformation directly gives the hopping parameters between ψ_3^- and $\psi_2^\pm$. All the allowed transitions are illustrated on an energy level diagram in Fig. 2(c).

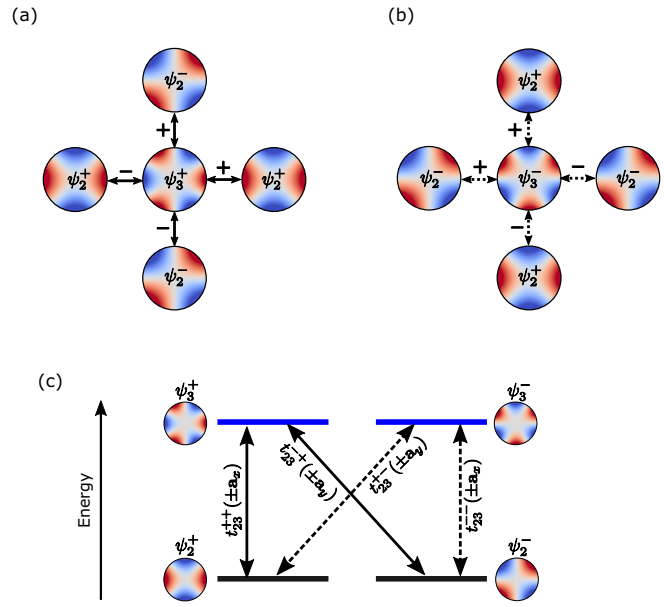

FIG. 2. Orbital coupling between $\psi_2^\pm$ and $\psi_3^\pm$. (a) Representation of nearest-neighbor hopping between ψ_3^+ and $\psi_2^\pm$. Hoppings for $\mathbf{R} = \pm\mathbf{a}_x, \pm\mathbf{a}_y$ are considered. The electric potential Φ of the modes is shown. The plus and minus signs associated with each hopping parameter indicate its sign. (b) Hopping between ψ_3^- and $\psi_2^\pm$. All hopping parameters for (b) can be generated by rotation of the configuration in (a). (c) The allowed hopping transitions are represented on an energy level diagram. A second-order transition connecting ψ_2^+ to ψ_2^- is possible via the $\psi_3^\pm$ modes.

Considering second-order hopping processes mediated by the $\psi_3^\pm$ orbital states, we find two processes that affect the quadrupole mode band structure. First, a second-order hopping along two links in the x or y directions [e.g., $t_{23}^{++}(\mathbf{a}_x)$ followed by $t_{32}^{++}(\mathbf{a}_x)$] provides a uniform shift in the energy of all orbital modes. A more interesting effect is found when a left or right turn is made between the first and second hops. Taking into account the signs given in Fig. 2, we arrive at an effective second-neighbor hopping between the quadrupole modes given by

$$W = it_s\sum_{pp'}\sum_{\langle\langle ij\rangle\rangle} v_{ij}c_{ip}^\dagger[\sigma_y]_{pp'}c_{jp'}, \tag{4}$$

where $v_{ij} = (\mathbf{d}_1 \times \mathbf{d}_2)_z$, $\mathbf{d}_{1,2}$ are the nearest-neighbor bonds connecting site i to j, $c_{ip}^\dagger$ is a creation operator for orbital ψ_2^p on lattice site i, and σ_y is a Pauli matrix acting on the quadrupole orbital degrees of freedom. This intrinsic interaction is analogous to the Kane-Mele spin-orbit interaction

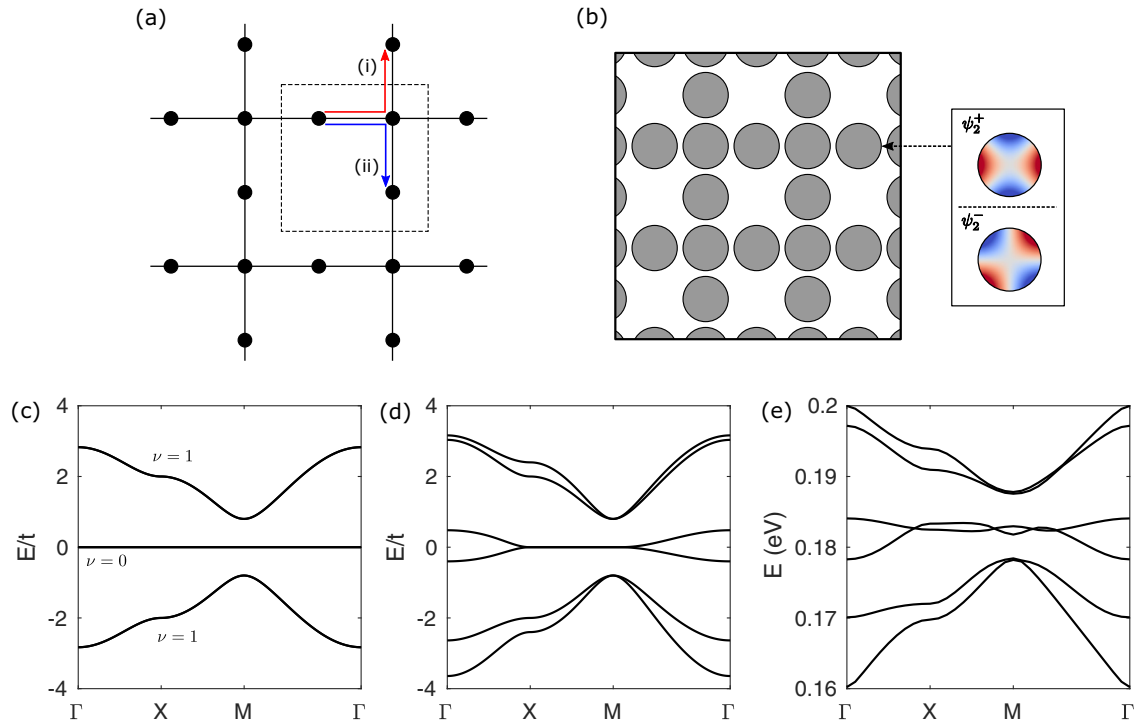

FIG. 3. Tight-binding mapping of a plasmonic Lieb lattice. (a) Tight-binding model onto which the plasmonic crystal can be mapped. The red and blue arrows represent two paths through which the interaction given by Eq. (4) connects a ψ_2^+ state to a ψ_2^- state. (b) Schematic representation of a graphene nanodisk Lieb lattice with ψ_2^+ and ψ_2^- orbitals on each site. Parameters are equivalent to the setup in Figs. 1(b), 1(c), and 1(d) Band structure calculated from the tight-binding model given in Eq. (5) with $\alpha = -1$ and $\alpha = -1.2$, respectively. For the $\alpha = -1$ case, the Z_2 topological invariant ν for each band is also shown. For the $\alpha = -1.2$ case, topologically trivial second-neighbor hopping is included. (e) Full wave electromagnetic simulation of plasmonic band structure for the configuration shown in (b).

discussed in the context of electronic systems [17]. Strength of the interaction t_s can be found by projecting the full Hamiltonian into an effective Hamiltonian in the $\psi_2^\pm$ basis. The effective Bloch Hamiltonian for the $\psi_2^\pm$ orbital basis may then be written as

$$h(\mathbf{k}) = \begin{pmatrix} h_+(\mathbf{k}) & w(\mathbf{k}) \\ w^\dagger(\mathbf{k}) & h_-(\mathbf{k}) \end{pmatrix} = \begin{pmatrix} h_+(\mathbf{k}) & w(\mathbf{k}) \\ w^\dagger(\mathbf{k}) & \alpha h_+(\mathbf{k}) \end{pmatrix}, \quad (5)$$

where $h_\pm$ is the intraorbital Hamiltonian for orbital $\psi_2^\pm$, α is the ratio between hopping amplitudes t_{22}^{++} and t_{22}^{--}, and w is a skew-Hermitian Hamiltonian that describes the effective second-neighbor coupling given by Eq. (4). Matrix representations of Eq. (5) are given in (see Supplemental Material [19]). With the effective Bloch Hamiltonian, we are able to map the quadrupole degrees of freedom of a plasmonic lattice onto a simple tight-binding model with two basis orbitals on each lattice site [see Figs. 3(a) and 3(b)].

For the ideal case with $\alpha = -1$ in Eq. (5), the Hamiltonian may be written as

$$h(\mathbf{k}) = h_+(\mathbf{k}) \otimes \sigma_z + w(\mathbf{k}) \otimes i\sigma_y. \quad (6)$$

The band structure for this Hamiltonian is shown in Fig. 3(c). A strict topological classification of this Hamiltonian based on its symmetries is possible. Define a synthetic time-reversal operator as $T = \lambda_z \otimes i\sigma_y K$, where $\lambda_z = \mathrm{diag}(1, -1, 1)$ is a sublattice symmetry operator acting on the sublattice degrees of freedom, σ_y is a Pauli matrix acting on the orbital degrees of freedom, and K represents complex conjugation. Then, the Hamiltonian in Eq. (6) satisfies $Th(\mathbf{k})T^{-1} = h(-\mathbf{k})$. Since $T^2 = -1$, a twofold degeneracy is enforced at the time-reversal invariant momenta by Kramer's theorem. A particle-hole symmetry operator can also be defined as $C = \sigma_x K$ such that $Ch(\mathbf{k})C^{-1} = -h(-\mathbf{k})$ and $C^2 = +1$. From the time-reversal and particle-hole symmetry, we can now place the $\alpha = -1$ Hamiltonian into the DIII symmetry class [20]. In two dimensions, this class is characterized by a Z_2 topological invariant. Since inversion symmetry is preserved, we may calculate the Z_2 invariant [21] ν of a single band by

$$(-1)^\nu = \prod_i \delta_i, \quad \delta_i = \xi(\Gamma_i), \quad (7)$$

where Γ_i are the time-reversal invariant momenta in the Brillouin zone and $\xi(\Gamma_i)$ is the parity eigenvalue of the band at Γ_i. Unlike the electronic case for which δ_i is given as a product of the parity eigenvalues for all occupied bands, here we associate a separate ν with each band individually since there is no notion of band filling. The Z_2 invariant for each band shown in Fig. 3(c) reveals the topologically nontrivial nature of the ideal plasmonic Lieb lattice.

Physically, $\alpha = -1$ requires fine tuning to a special state where the symmetry is strictly enforced. The plasmonic lattice comprised of disks does not have symmetries that require the $\alpha = -1$ condition. When $\alpha \neq -1$, classification of the system into the DIII class no longer holds and we do not have a sharp definition for the Z_2 topological invariant. In addition,

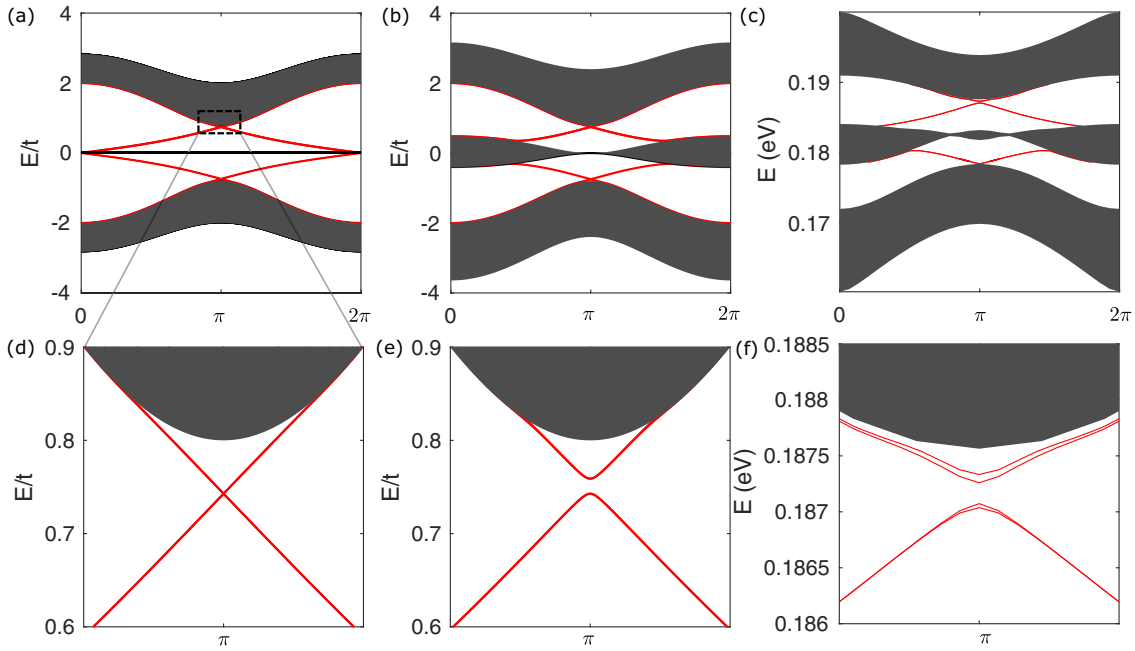

FIG. 4. Edge modes of the plasmonic Lieb lattice. (a), (d) Tight-binding band structure calculation for Lieb lattice in a ribbon geometry with $\alpha = -1$. The edge modes are highlighted in red, while the bulk band projections are colored in gray. All edge modes are doubly degenerate. A more detailed view of the crossing point of (a) is given in (d). (b), (e) Tight-binding band structure for $\alpha = -1.2$ and with topologically trivial second-neighbor hopping included. (c), (f) Full wave numerical simulation for plasmonic Lieb lattice in ribbon geometry. Parameters are identical to those used for Figs. 1(b) and 3(e).

topologically trivial intraorbital second-neighbor coupling (i.e., direct coupling along diagonal links in the Lieb lattice) is also present in the plasmonic lattice. Tight-binding calculations for the bulk band structure with $\alpha = -1.2$ and the trivial second-neighbor coupling are shown in Fig. 3(d). Breaking of the synthetic time-reversal symmetry is evident from the lifted degeneracy of the bulk bands at time reversal invariant momenta (TRIM) points Γ and X. The spectrum is also no longer symmetric with respect to $E = 0$ because particle-hole symmetry is broken by the topologically trivial second-neighbor hopping.

However, by examining the edge states of the physical $\alpha \neq -1$, we find that the topological signatures of the ideal lattice are still present. The spectrum of the edge modes can be studied in a finite-system ribbon geometry and shows that the edge modes from the ideal DIII structure [Fig. 4(a)] survive even when the strict symmetry classification breaks down [Fig. 4(b)]. A difference between the two cases is observed at the edge mode crossing points shown in Figs. 4(d) and 4(e) where the symmetry-broken case shows an avoided crossing originating from mixing of the edge modes. In principle, propagating edge modes near this crossing point will be able to backscatter. However, the size of the edge mode avoided crossing is roughly two orders of magnitude smaller than the band width, making it negligible in most practical situations. Full wave numerical simulations of the bulk plasmonic band structure shown in Fig. 3(e) confirm that while the $\alpha = -1$ condition is not strictly satisfied, the edge modes of topological origin still survive, as shown in Figs. 4(c) and 4(f).

To elucidate the properties of the edge modes, we apply a transformation into the angular momentum basis to Eq. (5). The angular momentum basis states are given by $\tilde{\psi}_m = \psi^+_{|m|} + i\mathrm{sgn}(m)\psi^-_{|m|}$, where the electric potential of $\tilde{\psi}_m$ is $\tilde{\Phi}_m(\mathbf{r}) \equiv u_0(r)e^{im\theta}$ and $m = \pm 1, \pm 2, \pm 3$. Applying the transformation to Eq. (5) gives the tight-binding Hamiltonian in the angular momentum basis,

$$\tilde{h}(\mathbf{k}) = \begin{pmatrix} \bar{h}(\mathbf{k}) + iw(\mathbf{k}) & \Delta(\mathbf{k}) \\ \Delta(\mathbf{k}) & \bar{h}(\mathbf{k}) - iw(\mathbf{k}) \end{pmatrix}, \tag{8}$$

where $\bar{h} = (h_+ + h_-)/2$ and $\Delta = (h_+ - h_-)/2$. Written in this form, it is clear that the plasmonic crystal will behave in a similar manner to the electronic quantum spin-Hall insulator, where the electronic spin degrees of freedom are mapped onto the chirality of the plasmon modes. The plasmonic edge modes observed in Fig. 4(f) will have a potential proportional to $e^{\pm i2\theta}$ on each disk where the chirality is tied to the propagation direction.

The existence of helical edge states can be confirmed by a simulation on a finite array of graphene disks. In order to couple with the $\tilde{\psi}_{-2}$ angular momentum mode, we use a circularly polarized dipole with dipole moment $\mathbf{p} = \hat{\mathbf{x}} + i\hat{\mathbf{y}}$ placed at the edge of an A-site graphene disk. Simulation results in Fig. 5 show a projection of the excited plasmon fields onto the $\tilde{\psi}_{\pm 2}$ modes. We find that the dipole strongly couples to a $\tilde{\psi}_{-2}$ mode which propagates counterclockwise along the boundaries of the system. A weak excitation of $\tilde{\psi}_{+2}$ is caused by imperfect coupling between the circularly polarized dipole and the $\tilde{\psi}_{-2}$ mode.

We now identify perturbations that open a topologically trivial gap at the M point and may occur in an array of

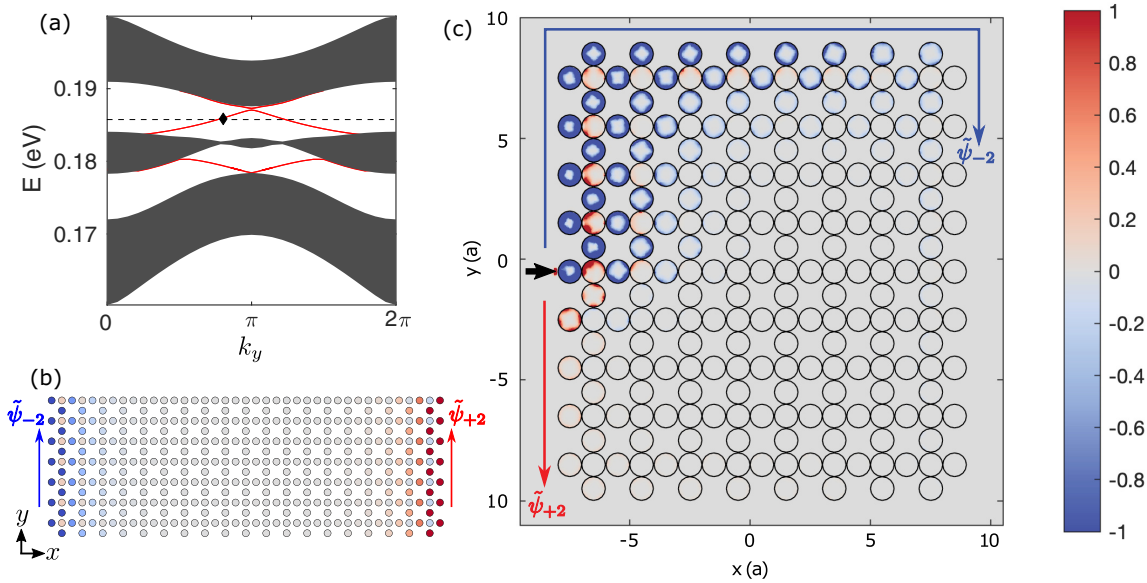

FIG. 5. Dipole launching the edge states of the plasmonic Lieb lattice. (a) Band structure of the plasmonic Lieb lattice in a ribbon geometry. Bands traversing the bulk gap are all doubly degenerate. (b) Schematic representation of the eigenstate corresponding to the black diamond in (a). The blue (red) shows projection onto state $\tilde{\psi}_{-2}$ ($\tilde{\psi}_{+2}$). Arrows indicate the group velocity of each edge mode. (c) Simulation of topological edge plasmon launched by circularly polarized dipole at frequency indicated in (a). Magnitude of the plasmon electric field is multiplied by a projection onto the $\tilde{\psi}_{\pm 2}$ angular momentum states. Dipole source is placed at the black arrow 5 nm above the graphene nanodisk.

plasmonic disks. The first is an inversion-breaking perturbation which may result from an asymmetric hopping along either the x or y links in the lattice. A shift of the A- or C-site plasmonic disk towards the B site will give rise to the inversion-breaking perturbation. Shifting the B-site energy also opens up a gap on one side of the flat bands. A shift in the Fermi energy of the plasmonic disk will result in this type of perturbation. When applying either of the above-mentioned perturbations to an ideal DIII class system, the edge modes are removed only after the gap closes and reopens. Interestingly, even in the physical case where we are no longer in the ideal DIII class, the edge modes persist until the gap is closed, implying that the edge modes remain robust to external perturbations over a wide parameter range (see Supplemental Material [19]).

Experimentally, the proposed helical edge modes can be excited by placing a near-field antenna at the edge of the plasmon disk array, as shown in Fig. 5(c). For the setup used in this work, the gap in which the edge mode can be observed is 4 meV. We expect the edge mode in this gap to be observable as a plasmonic band gap of similar size has been successfully resolved using the near-field scanning microscope technique [14]. Furthermore, the line widths of the plasmonic band structure reveal that the band gap can be resolved even in the presence of realistic losses. The energy scale of the plasmonic band structure can also be shifted by simply scaling the geometry of the lattice. For a disk size of $d = 700$ nm and periodicity $a = 735$ nm, the quadrupole band energies are lowered to 70 meV. Importantly, the ratio between the bandwidth and band gap stays constant as the geometry is scaled. Hence the physical phenomena that we have examined for the setup in this work can be translated to a different energy range by scaling the geometry accordingly. Finally, imperfections in disk fabrication may result in a slight breaking of the rotational symmetry of the multipolar modes. Even with slight rotational symmetry breaking, we find that the band gap is not closed and that the edge modes are still observable within the band gap (see Supplemental Material [19]).

Conclusion. In summary, we have shown that propagating helical edge modes induced by an intrinsic synthetic spin-orbit process exists in an artificial plasmonic crystal. We consider the Lieb lattice as a prototypical example and develop a mapping of the plasmonic system onto a simple tight-binding model. With the tight-binding model, we identify an ideal limit of the system in which it can be classified into the DIII symmetry class. In this limit, a nontrivial Z_2 invariant is calculated and the associated topologically protected edge states are shown to exist. It is important to note that this ideal limit is distinct from the case of electron spins on a Lieb lattice and is a result of the opposite sign hopping between the localized plasmon modes. Although the physical plasmonic lattice does not strictly follow the behavior of this ideal limit, we are able to verify that the system is close enough to retain the edge states found for the ideal DIII limit. Propagation of the helical plasmonic edge modes is verified using full wave numerical simulations. Further engineering of the substrate or fine tuning of the disk shapes may lead to a realization of the ideal DIII limit.

Methods. All electromagnetic simulations were performed using COMSOL MULTIPHYSICS. Graphene is modeled as a surface current with a Drude conductivity, $\sigma(\omega) = \frac{e^2}{\pi\hbar}\frac{E_F}{\hbar\gamma - i\hbar\omega}$. Scattering time is set to $\tau = 1$ ps, where $\gamma = 1/\tau$. The bulk plasmonic band structure shown in Figs. 1 and 3 was performed by assuming periodic boundary conditions along both of the in-plane directions. In the out-of-plane direction, the structure is padded with 1 μm of free space and a perfectly

matched layer of thickness 300 nm. The plasmonic band structure calculation for a ribbon geometry, shown in Figs. 4(c) and 4(f), was performed using a ribbon length of 25 unit cells with periodic boundary conditions only in the direction parallel to the ribbon edges. The circularly polarized dipole used for Fig. 5(c) was placed 5 nm above the edge of the graphene nanodisk. Projection of the potential onto the angular momentum states $\tilde{\psi}_{\pm 2}$ was calculated as $\int e^{i2\theta} \Phi(\mathbf{r})/|\Phi(\mathbf{r})| d^2r - \int e^{-i2\theta} \Phi(\mathbf{r})/|\Phi(\mathbf{r})| d^2r$ for each disk.

Acknowledgments. S.H.P., M.S., and T.L. acknowledge support by the National Science Foundation, NSF/EFRI Grant No. EFRI-1741660. Work by E.J.M. was supported by the Department of Energy under Grant No. DE-FG02-84ER45118. S.H.P. acknowledges partial support by the National Science Foundation through the University of Minnesota MRSEC under Award No. DMR-2011401. S.H.P. and T.L. acknowledge partial support from the Office of Naval Research MURI Grant No. N00014-23-1-2567.

[1] J. D. Joannapoulos, S. G. Johnson, J. N. Winn, and R. D. Meade, *Photonic Crystals: Molding the Flow of Light*, 2nd ed. (Princeton University Press, Princeton, NJ, 2011).
[2] L. Lu, J. D. Joannopoulos, and M. Soljačić, Topological photonics, Nat. Photon. **8**, 821 (2014).
[3] A. B. Khanikaev and G. Shvets, Two-dimensional topological photonics, Nat. Photon. **11**, 763 (2017).
[4] M. Z. Hasan and C. L. Kane, *Colloquium:* Topological insulators, Rev. Mod. Phys. **82**, 3045 (2010).
[5] Z. Wang, Y. Chong, J. D. Joannopoulos, and M. Soljačić, Observation of unidirectional backscattering-immune topological electromagnetic states, Nature (London) **461**, 772 (2009).
[6] D. Jin, T. Christensen, M. Soljačić, N. X. Fang, L. Lu, and X. Zhang, Infrared topological plasmons in graphene, Phys. Rev. Lett. **118**, 245301 (2017).
[7] L. M. Nash, D. Kleckner, A. Read, V. Vitelli, A. M. Turner, and W. T. M. Irvine, Topological mechanics of gyroscopic metamaterials, Proc. Natl. Acad. Sci. USA **112**, 14495 (2015).
[8] L. Lu, J. D. Joannopoulos, and M. Soljačić, Topological states in photonic systems, Nat. Phys. **12**, 626 (2016).
[9] M. Hafezi, E. A. Demler, M. D. Lukin, and J. M. Taylor, Robust optical delay lines with topological protection, Nat. Phys. **7**, 907 (2011).
[10] A. B. Khanikaev, S. H. Mousavi, W.-K. Tse, M. Kargarian, A. H. MacDonald, and G. Shvets, Photonic topological insulators, Nat. Mater. **12**, 233 (2012).
[11] L.-H. Wu and X. Hu, Scheme for achieving a topological photonic crystal by using dielectric material, Phys. Rev. Lett. **114**, 223901 (2015).
[12] D. Pan, R. Yu, H. Xu, and F. J. García de Abajo, Topologically protected Dirac plasmons in a graphene superlattice, Nat. Commun. **8**, 1243 (2017).
[13] M. Jung, Z. Fan, and G. Shvets, Midinfrared plasmonic valleytronics in metagate-tuned graphene, Phys. Rev. Lett. **121**, 086807 (2018).
[14] L. Xiong *et al.*, Photonic crystal for graphene plasmons, Nat. Commun. **10**, 4780 (2019).
[15] C. Weeks and M. Franz, Topological insulators on the Lieb and perovskite lattices, Phys. Rev. B **82**, 085310 (2010).
[16] N. Goldman, D. F. Urban, and D. Bercioux, Topological phases for fermionic cold atoms on the Lieb lattice, Phys. Rev. A **83**, 063601 (2011).
[17] C. L. Kane and E. J. Mele, Z_2 topological order and the quantum spin Hall effect, Phys. Rev. Lett. **95**, 146802 (2005).
[18] I. Silveiro, A. Manjavacas, S. Thongrattanasiri, and F. J. García de Abajo, Plasmonic energy transfer in periodically doped graphene, New J. Phys. **15**, 033042 (2013).
[19] See Supplemental Material at http://link.aps.org/supplemental/10.1103/PhysRevB.109.L161301 for a detailed discussion of tight-binding formulation, perturbations, and experimental considerations.
[20] C.-K. Chiu, J. C. Y. Teo, A. P. Schnyder, and S. Ryu, Classification of topological quantum matter with symmetries, Rev. Mod. Phys. **88**, 035005 (2016).
[21] L. Fu and C. L. Kane, Topological insulators with inversion symmetry, Phys. Rev. B **76**, 045302 (2007).